Calculation of the SAR Induced in Head Tissues Using a High-Order DGTD Method and Triangulated Geometrical Models

Hassan Fahs, Abdelhamid Hadjem, Stéphane Lanteri, Joe Wiart, *Senior Member, IEEE*, and Man-Fai Wong, *Senior Member, IEEE*

***Abstract*—The great majority of numerical calculations of the specific absorption rate (SAR) induced in human tissues exposed to microwaves are performed using the finite difference time-domain (FDTD) method and voxel-based geometrical models. The straightforward implementation of the method and its computational efficiency are among the main reasons for FDTD being currently the leading method for numerical assessment of human exposure to electromagnetic waves. However, the rather difficult departure from the commonly used Cartesian grid and cell size limitations regarding the discretization of very detailed structures of human tissues are often recognized as the main weaknesses of the method in this application context. In particular, interfaces between tissues where sharp gradients of the electromagnetic field may occur are hardly modeled rigorously in these studies. We present here an alternative numerical dosimetry methodology which is based on a high order discontinuous Galerkin time-domain (DGTD) method and adapted geometrical models constructed from unstructured triangulations of tissue interfaces, and discuss its application to the calculation of the SAR induced in head tissues.**

***Index Terms*—Discontinuous Galerkin, finite element, time-domain Maxwell's equations, numerical dosimetry, unstructured meshes.**

I. Introduction

NOWADAYS, numerical modeling is increasingly used and progressively becoming a mandatory path for the study of the interaction of electromagnetic fields with biological tissues. This is in particular the case for the evaluation of the specific absorption rate (SAR) which is a measure of the rate at which electric energy is absorbed by the tissues when exposed to a radio-frequency electromagnetic field. The SAR is defined as the power absorbed per mass of tissue and has units of watts per kilogram. Numerical SAR calculations are intensively considered for dosimetric studies of the exposure of human tissues to microwave radiations from wireless communication systems [1]–[3] to cite but a few of many examples. These studies are useful for assessing the possible thermal effects (temperature rise in tissues resulting from electric energy dissipation) as well as for compliance testing to regulatory limits. SAR calculations are also relevant for certain medical applications such as for the design of microwave hyperthermia systems [4]–[6] and for the design of micro-antennas to be implanted inside the human body [7].

Despite the high complexity both in terms of heterogeneity and geometrical features of tissues, the great majority of numerical dosimetry studies have been conducted using the widely known finite difference time-domain (FDTD) method due to Yee [8]. In this method, the whole computational domain is discretized using a structured (Cartesian) grid. Due to the possible straightforward implementation of the algorithm and the availability of computational power, FDTD is currently the leading method for numerical assessment of human exposure to electromagnetic waves. In the particular case of mobile phone radiation, the FDTD method is applied to heterogeneous discretized models of human head tissues built from medical images. Thus, the grid generation process is highly simplified since the voxel-based image can be used at a minimal effort as the computational grid for the FDTD method. In spite of its flexibility and second-order accuracy in a homogeneous medium, the Yee scheme suffers from serious accuracy degradation when used to model curved objects or when treating material interfaces. Indeed, the so-called stair-casing approximation may lead to local zeroth-order and at most first-order accuracy; it may also produce locally non-convergent results [9]. Furthermore, for Maxwell's equations with discontinuous coefficients, the Yee scheme might not be able to capture the possible discontinuity of the solution across the interfaces [9]. A number of finite difference methods have been proposed in the past for the treatment of curved interfaces. The usual and straightforward approach is to introduce local modifications into the Yee scheme but still keep the staggered grid [10], [11], or to use local mesh refinements [12], [13]. Some studies have been concerned with high-order embedded FDTD schemes in the presence of material interfaces [14], including the staggered fourth-order accurate methods by Yefet *et al.* [15], and the fourth-order orthogonal curvilinear staggered grid methods by Xie *et al.* [16]. Most of these methods, however, have not really penetrated into main stream user community, partly due to

Manuscript received May 03, 2010; revised December 21, 2010, April 11, 2011; accepted June 02, 2011. Date of publication August 18, 2011; date of current version December 02, 2011.

H. Fahs was with the Nachos Project-Team, INRIA Sophia Antipolis-Méditerranée Research Center, 06902 Sophia Antipolis Cedex, France. He is now with the OSA Department, XLIM Institute, 87060 Limoges, France (e-mail: hassan.fahs@gmail.com).

S. Lanteri is with the Nachos Project-Team, INRIA Sophia Antipolis-Méditerranée Research Center, 06902 Sophia Antipolis Cedex, France (e-mail: stephane.lanteri@inria.fr).

A. Hadjem and J. Wiart are with France Telecom R&D, WHIST Laboratory, 92794 Issy-les-Moulineaux Cedex 9, France (e-mail: abdelhamid.hadjem@orange-ftgroup.com; joe.wiart@orange-ftgroup.com).

M.-F. Wong, deceased, was with France Telecom R&D, Whist Laboratory, 92794 Issy-les-Moulineaux Cedex 9, France

Color versions of one or more of the figures in this paper are available online at http://ieeexplore.ieee.org.

Digital Object Identifier 10.1109/TAP.2011.2165471

their complicated nature and partly because these new methods themselves often introduce other complications.

In an attempt to offer an alternative numerical dosimetry methodology which allows for a realistic modeling of geometrical features and tissue interfaces, we consider here the use of a discontinuous finite element method formulated on nonuniform tetrahedral meshes. The method is known as the discontinuous Galerkin method and has been studied by several authors rather recently for solving the time-domain Maxwell equations [17]–[19]. Discontinuous Galerkin time-domain (DGTD) methods based on discontinuous finite element spaces, easily handle elements of various types and shapes, irregular nonconforming meshes [20], and even locally varying polynomial degree, and hence offer great flexibility in the mesh design. They also lead to (block-) diagonal mass matrices and therefore yield fully explicit, inherently parallel methods when coupled with explicit time stepping. Moreover, continuity is weakly enforced across mesh interfaces by adding suitable bilinear forms (so-called numerical fluxes) to the standard variational formulations. The DGTD method that we consider here is a preliminary extension to the three-dimensional case of the one presented in [20].

Similarly to the FDTD based numerical dosimetry methodologies, the DGTD method considered here relies on geometrical models built from medical images. However, in the present case, the viewpoint that we adopt is to use realistic geometrical models of head tissues whose construction is constrained by triangulations of interfaces between different tissues, that are extracted from appropriately segmented MR images. In practice, this can be achieved for a limited number of tissues thus implying that a form of homogeneization is applied to the remaining tissues. In this context, one objective of this work is to study numerically the possibility of using adapted geometrical models consisting of locally refined/coarsened tetrahedral meshes, constructed from the extracted set of triangulated tissue interfaces. In addition, since the computational domains under consideration also involve a free space propagation region external to the head, we also explore a numerical modeling strategy which combines a structured (i.e., uniform) tetrahedral mesh for the propagation in the free space region, with a fully unstructured tetrahedral mesh for the propagation in the head tissues. Such meshes, whether they are globally conforming or not (i.e., with hanging nodes) can be easily handled by a discontinuous Galerkin formulation, as can be a local definition (i.e., element-wise) of approximation order of the electromagnetic field. This feature is also exploited in the present study with the overall objective to reduce the computing time while preserving an acceptable accuracy with reference to a high-resolution numerical solution computed on globally refined mesh.

The rest of the paper is organized as follows: the initial and boundary value problem at hand and its DGTD discretization are presented in Section II; in Section III we describe the strategy used for the construction of realistic geometrical models of head tissues based on surface triangulations and volumic tetrahedral meshes; numerical results are presented in Section IV; finally, Section V concludes this work and sets some future research directions.

II. DGTD Method on Tetrahedral Meshes

A. Continuous Problem

We consider the Maxwell equations in three space dimensions for heterogeneous linear isotropic media. The electric field $\vec{E}(\vec{x},t) = {}^t(E_x, E_y, E_z)$ and the magnetic field $\vec{H}(\vec{x},t) = {}^t(H_x, H_y, H_z)$ verify

$$\epsilon\partial_t\vec{E} - \mathrm{curl}\vec{H} = -\vec{J}, \mu\partial_t\vec{H} + \mathrm{curl}\vec{E} = 0 \qquad (1)$$

where the symbol ∂_t denotes a time derivative and $\vec{J}(\vec{x},t)$ is a current source term. These equations are set on a bounded polyhedral domain Ω of $\mathbb{R}^3$. The electric permittivity $\epsilon(\vec{x})$ and the magnetic permeability coefficients $\mu(\vec{x})$ are varying in space, time-invariant and both positive functions. The current source term $\vec{J}$ is the sum of the conductive current $\vec{J}_\sigma = \sigma\vec{E}$ (where $\sigma(\vec{x})$ denotes the electric conductivity of the media) and of an applied current $\vec{J}_s$ associated to a localized source for the incident electromagnetic field. Our goal is to solve system (1) in a domain Ω with boundary $\partial\Omega = \Gamma_a \cup \Gamma_m$, where we impose the following boundary conditions: $\vec{n}\times\vec{E} = 0$ on Γ_m, and $\mathcal{L}(\vec{E},\vec{H}) = \mathcal{L}(\vec{E}_{\mathrm{inc}},\vec{H}_{\mathrm{inc}})$ on Γ_a where $\mathcal{L}(\vec{E},\vec{H}) = \vec{n}\times\vec{E} - \sqrt{(\mu)/(\varepsilon)}\vec{n}\times(\vec{H}\times\vec{n})$. Here $\vec{n}$ denotes the unit outward normal to $\partial\Omega$ and $(\vec{E}_{\mathrm{inc}},\vec{H}_{\mathrm{inc}})$ is a given incident field. The first boundary condition is called *metallic* (referring to a perfectly conducting surface) while the second condition is called *absorbing* and takes here the form of the Silver–Müller condition which is a first order approximation of the exact absorbing boundary condition. This absorbing condition is applied on Γ_a which represents an artificial truncation of the computational domain.

B. Space Discretization

We consider a partition $\mathcal{T}_h$ of Ω into a set of tetrahedra τ_i of size h_i with boundary $\partial\tau_i$ such that $h = \max_{\tau_i\in\mathcal{T}_h} h_i$. To each $\tau_i \in \mathcal{T}_h$, we assign a non-negative integer p_i that is the local interpolation degree. For each τ_i, the parameters ϵ_i and μ_i are respectively the local electric permittivity and magnetic permeability of the medium, which are assumed constant inside the element τ_i. For two distinct tetrahedra τ_i and τ_k in $\mathcal{T}_h$, the intersection $\tau_i\cap\tau_k$ is a convex polyhedron a_{ik} which we will call interface. For each internal interface a_{ik}, we denote by $\vec{n}_{ik}$ the unitary normal vector, oriented from τ_i to τ_k. For the boundary interfaces, the index k corresponds to a fictitious element outside the domain. We denote by $\mathcal{F}_h^I$ the union of all interior interfaces of $\mathcal{T}_h$ and by $\mathcal{F}_h^B$ the union of all boundary interfaces of $\mathcal{T}_h$. Finally, we denote by $\mathcal{V}_i$ the set of indices of the elements which are neighbors of τ_i (having an interface in common). In the following, to simplify the presentation, we set $\vec{J} = 0$. For a given partition $\mathcal{T}_h$, we seek approximate solutions to (1) in the finite element space

$$V_{p_i}(\mathcal{T}_h) = \{\vec{v}\in L^2(\Omega)^3 : \vec{v}_{|\tau_i} \in (\mathbb{P}_{p_i}[\tau_i])^3,\ \forall\tau_i\in\mathcal{T}_h\} \qquad (2)$$

where $\mathbb{P}_{p_i}[\tau_i]$ denotes the space of nodal polynomial functions of degree at most p_i inside τ_i. Following the discontinuous Galerkin approach, the local electric and magnetic fields $(\vec{\mathbf{E}}_i,\vec{\mathbf{H}}_i)$ are defined as combinations of linearly independent

basis vector fields $\vec{\varphi}_{ij}$. Let $\mathcal{P}_i = \mathrm{Span}(\vec{\varphi}_{ij}, 1 \leq j \leq d_i)$ where d_i denotes the number of degrees of freedom inside τ_i. The approximate fields $(\vec{\mathbf{E}}_h, \vec{\mathbf{H}}_h)$, defined by $(\forall i, \vec{\mathbf{E}}_{h|\tau_i} = \vec{\mathbf{E}}_i, \vec{\mathbf{H}}_{h|\tau_i} = \vec{\mathbf{H}}_i)$ are allowed to be completely discontinuous across element boundaries. For such a discontinuous field $\vec{\mathbf{U}}_h$, we define its average $\{\vec{\mathbf{U}}_h\}_{ik}$ through any internal interface a_{ik}, as $\{\vec{\mathbf{U}}_h\}_{ik} = (\vec{\mathbf{U}}_{i|a_{ik}} + \vec{\mathbf{U}}_{k|a_{ik}})/2$. Note that for any internal interface a_{ik}, $\{\vec{\mathbf{U}}_h\}_{ki} = \{\vec{\mathbf{U}}_h\}_{ik}$. Because of this discontinuity, a global variational formulation cannot be obtained. However, dot-multiplying (1) by $\vec{\varphi} \in \mathcal{P}_i$, integrating over each single element τ_i and integrating by parts, yields

$$\begin{cases} \displaystyle\int_{\tau_i} \vec{\varphi} \cdot \epsilon_i \partial_t \vec{\mathbf{E}} = \int_{\tau_i} \mathrm{curl}\vec{\varphi} \cdot \vec{\mathbf{H}} - \int_{\partial\tau_i} \vec{\varphi} \cdot (\vec{\mathbf{H}} \times \vec{n}) \\ \displaystyle\int_{\tau_i} \vec{\varphi} \cdot \mu_i \partial_t \vec{\mathbf{H}} = -\int_{\tau_i} \mathrm{curl}\vec{\varphi} \cdot \vec{\mathbf{E}} + \int_{\partial\tau_i} \vec{\varphi} \cdot (\vec{\mathbf{E}} \times \vec{n}). \end{cases} \tag{3}$$

In (3), we now replace the exact fields $\vec{\mathbf{E}}$ and $\vec{\mathbf{H}}$ by the approximate fields $\vec{\mathbf{E}}_h$ and $\vec{\mathbf{H}}_h$ in order to evaluate volume integrals. For integrals over $\partial\tau_i$, a specific treatment must be introduced since the approximate fields are discontinuous through element faces, leading to the definition of a *numerical flux*. We choose to use a fully centered numerical flux, i.e., $\forall i, \forall k \in \mathcal{V}_i, \vec{\mathbf{E}}_{|a_{ik}} \simeq \{\vec{\mathbf{E}}_h\}_{ik}, \vec{\mathbf{H}}_{|a_{ik}} \simeq \{\vec{\mathbf{H}}_h\}_{ik}$. The metallic boundary condition on a boundary interface $a_{ik} \in \Gamma_m$ (k in the element index of the fictitious neighboring element) is dealt with *weakly*, in the sense that traces of fictitious fields $\vec{\mathbf{E}}_k$ and $\vec{\mathbf{H}}_k$ are used for the computation of numerical fluxes for the boundary element τ_i. More precisely, we set $\vec{\mathbf{E}}_{k|a_{ik}} = -\vec{\mathbf{E}}_{i|a_{ik}}$ and $\vec{\mathbf{H}}_{k|a_{ik}} = \vec{\mathbf{H}}_{i|a_{ik}}$. Similarly, the absorbing boundary condition is taken into account through the use of a fully upwind numerical flux for the evaluation of the corresponding boundary integral over $a_{ik} \in \Gamma_a$ (see [18] for more details). Evaluating the surface integrals in (3) using the centered numerical flux, and reintegrating by parts yields

$$\begin{cases} \displaystyle\int_{\tau_i} \vec{\varphi} \cdot \epsilon_i \partial_t \vec{\mathbf{E}}_i = \frac{1}{2}\int_{\tau_i} (\mathrm{curl}\vec{\varphi} \cdot \vec{\mathbf{H}}_i + \mathrm{curl}\vec{\mathbf{H}}_i \cdot \vec{\varphi}) \\ \qquad\qquad -\dfrac{1}{2}\displaystyle\sum_{k\in\mathcal{V}_i} \int_{a_{ik}} \vec{\varphi} \cdot (\vec{\mathbf{H}}_k \times \vec{n}_{ik}) \\ \displaystyle\int_{\tau_i} \vec{\varphi} \cdot \mu_i \partial_t \vec{\mathbf{H}}_i = -\frac{1}{2}\int_{\tau_i} (\mathrm{curl}\vec{\varphi} \cdot \vec{\mathbf{E}}_i + \mathrm{curl}\vec{\mathbf{E}}_i \cdot \vec{\varphi}) \\ \qquad\qquad +\dfrac{1}{2}\displaystyle\sum_{k\in\mathcal{V}_i} \int_{a_{ik}} \vec{\varphi} \cdot (\vec{\mathbf{E}}_k \times \vec{n}_{ik}). \end{cases} \tag{4}$$

Equation (4) can be rewritten in terms of scalar unknowns. Inside each element, the fields are recomposed according to $\vec{\mathbf{E}}_i = \sum_{1\leq j\leq d} E_{ij}\vec{\varphi}_{ij}$ and $\vec{\mathbf{H}}_i = \sum_{1\leq j\leq d} H_{ij}\vec{\varphi}_{ij}$ and let us now denote by $\mathbf{E}_i$ and $\mathbf{H}_i$ respectively the column vectors $(E_{il})_{1\leq l\leq d_i}$ and $(H_{il})_{1\leq l\leq d_i}$. Then, (4) is equivalent to

$$\begin{cases} M_i^\epsilon \frac{d\mathbf{E}_i}{dt} = K_i\mathbf{H}_i - \displaystyle\sum_{k\in\mathcal{V}_i} S_{ik}\mathbf{H}_k \\ M_i^\mu \frac{d\mathbf{H}_i}{dt} = -K_i\mathbf{E}_i + \displaystyle\sum_{k\in\mathcal{V}_i} S_{ik}\mathbf{E}_k \end{cases} \tag{5}$$

where the symmetric positive definite mass matrices M_i^η (η stands for ϵ or μ), the symmetric stiffness matrix K_i (both of size $d_i \times d_i$) and the symmetric interface matrix S_{ik} (of size $d_i \times d_k$) are given by

$$\begin{aligned} (M_i^\eta)_{jl} &= \eta_i \int_{\tau_i} {}^t\vec{\varphi}_{ij} \cdot \vec{\varphi}_{il} \\ (K_i)_{jl} &= \frac{1}{2}\int_{\tau_i} {}^t\vec{\varphi}_{ij} \cdot \mathrm{curl}\vec{\varphi}_{il} + {}^t\vec{\varphi}_{il} \cdot \mathrm{curl}\vec{\varphi}_{ij}, \\ (S_{ik})_{jl} &= \frac{1}{2}\int_{a_{ik}} {}^t\vec{\varphi}_{ij} \cdot (\vec{\varphi}_{kl} \times \vec{n}_{ik}). \end{aligned}$$

C. Time Discretization

The set of local system of ordinary differential equations for each τ_i (5) can be formally transformed in a global system. To this end, we suppose that all electric (resp. magnetic) unknowns are gathered in a column vector $\mathbb{E}$ (resp. $\mathbb{H}$) of size $d_g = \sum_{i=1}^{N_t} d_i$ where N_t stands for the number of elements in $\mathcal{T}_h$. Then system (5) can be rewritten as

$$\begin{cases} \mathbb{M}^\epsilon \frac{d\mathbb{E}}{dt} = \mathbb{K}\mathbb{H} - \mathbb{A}\mathbb{H} - \mathbb{B}\mathbb{H} + \mathbb{C}_E\mathbb{E}, \\ \mathbb{M}^\mu \frac{d\mathbb{H}}{dt} = -\mathbb{K}\mathbb{E} + \mathbb{A}\mathbb{E} - \mathbb{B}\mathbb{E} + \mathbb{C}_H\mathbb{H} \end{cases} \tag{6}$$

where we have the following definitions and properties:

- $\mathbb{M}^\epsilon, \mathbb{M}^\mu$ and $\mathbb{K}$ are $d_g \times d_g$ block diagonal matrices with diagonal blocks equal to M_i^ϵ, M_i^μ and K_i respectively. $\mathbb{M}^\epsilon$ and $\mathbb{M}^\mu$ are symmetric positive definite matrices, and $\mathbb{K}$ is a symmetric matrix.
- $\mathbb{A}$ is also a $d_g \times d_g$ block sparse matrix, whose nonzero blocks are equal to S_{ik} when $a_{ik} \in \mathcal{F}_h^I$. Since $\vec{n}_{ki} = -\vec{n}_{ik}$, it can be checked that $(S_{ik})_{jl} = (S_{ki})_{lj}$ and then $S_{ki} = {}^tS_{ik}$; thus, $\mathbb{A}$ is a symmetric matrix.
- $\mathbb{B}$ is a $d_g \times d_g$ block diagonal matrix, whose nonzero blocks are equal to S_{ik} when $a_{ik} \in \mathcal{F}_h^B \cap \Gamma_m$. In that case, $(S_{ik})_{jl} = -(S_{ik})_{lj}$; thus, $\mathbb{B}$ is a skew-symmetric matrix.
- $\mathbb{C}_E$ and $\mathbb{C}_H$ are $d_g \times d_g$ block diagonal matrices associated to boundary integral terms for $a_{ik} \in \mathcal{F}_h^B \cap \Gamma_a$.

Consequently, if we set $\mathbb{S} = \mathbb{K} - \mathbb{A} - \mathbb{B}$, the system (6) rewrites as

$$\mathbb{M}^\epsilon \frac{d\mathbb{E}}{dt} = \mathbb{S}\mathbb{H} + \mathbb{C}_E\mathbb{E}, \mathbb{M}^\mu \frac{d\mathbb{H}}{dt} = -{}^t\mathbb{S}\mathbb{E} + \mathbb{C}_H\mathbb{H}. \tag{7}$$

The semi-discrete system (7) is time integrated using a second-order leap-frog scheme as

$$\begin{cases} \mathbb{M}^\epsilon \left(\frac{\mathbb{E}^{n+1} - \mathbb{E}^n}{\Delta t}\right) = \mathbb{S}\mathbb{H}^{n+\frac{1}{2}} + \mathbb{C}_E\mathbb{E}^n, \\ \mathbb{M}^\mu \left(\frac{\mathbb{H}^{n+\frac{3}{2}} - \mathbb{H}^{n+\frac{1}{2}}}{\Delta t}\right) = -{}^t\mathbb{S}\mathbb{E}^{n+1} + \mathbb{C}_H\mathbb{H}^{n+\frac{1}{2}}. \end{cases} \tag{8}$$

The resulting fully explicit DGTD-$\mathbb{P}_{p_i}$ method is analyzed in [18] where it is shown that, when $\Gamma_a = \emptyset$, the method is non-dissipative, conserves a discrete form of the electromagnetic energy and is stable under the CFL-like condition

$$\Delta t \leq \frac{2}{\alpha}, \text{ with } \alpha = \left\| (\mathbb{M}^{-\mu})^{\frac{1}{2}}\, {}^t\mathbb{S}\, (\mathbb{M}^{-\epsilon})^{\frac{1}{2}} \right\| \tag{9}$$

where $\|\cdot\|$ denotes the canonical matrix norm and the matrix $(\mathbb{M}^{-\eta})^{(1)/(2)}$ is the inverse square root of $\mathbb{M}^\eta$.

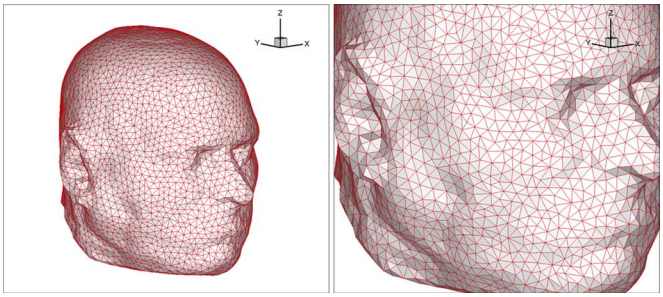

Fig. 1. Surface mesh of the skin.

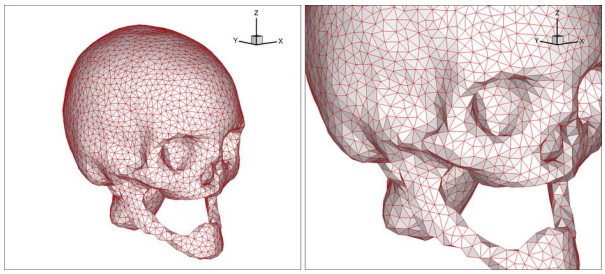

Fig. 2. Surface mesh of the skull.

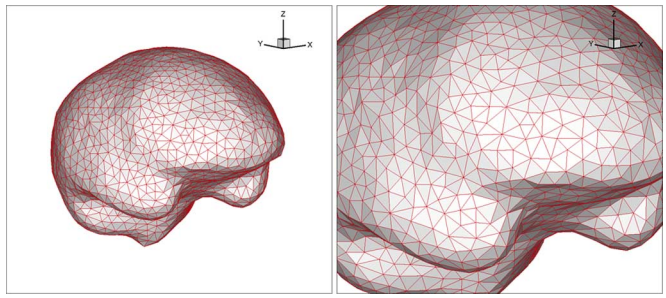

Fig. 3. Surface mesh of the brain.

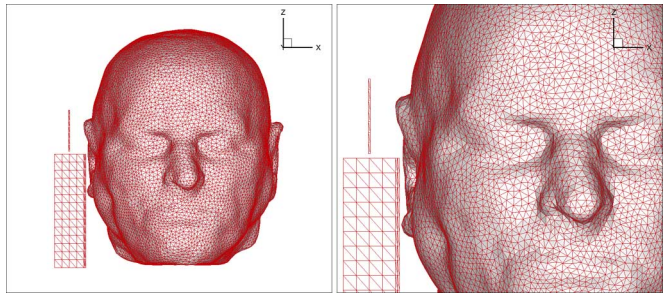

Fig. 4. Simplified mobile phone model and its positioning.

D. Numerical Treatment of Conductive Materials

Human tissues are conductive materials and thus require that a conductive current $\vec{J}_\sigma = \sigma\vec{E}$ is taken into account in (1). It is straightforward to verify that the space discretization of this current term in the framework of the discontinuous Galerkin formulation described in Section II-B leads to the introduction of the term $-M_i^\epsilon \mathbf{E}_i$ in the right-hand side of the first equation of (5). Then this term is time integrated as $-M_i^\epsilon(\mathbf{E}_i^n + \mathbf{E}_i^{n+1})/2$ meaning that both the left- and right-hands side terms of (8) are affected by the discretization of this conductive current.

III. Tetrahedral Mesh-Based Geometric Models of Head Tissues

The DGTD-$\mathbb{P}_{p_i}$ method described previously assumes that the computational domain is discretized using tetrahedral elements. In this study, we aim at exploiting this numerical method for the calculation of the SAR induced in head tissues. A first step is thus to construct compatible geometrical models of the head tissues. Starting from magnetic resonance images of the Visible Human 2.0 project [21], head tissues are segmented and the interfaces of a selected number of tissues are triangulated. Different strategies can be used in order to obtain a smooth and accurate segmentation of head tissues and interface triangulations as well. The strategy adopted in this work consists in using a variant of Chew's algorithm [22], based on Delaunay triangulation restricted to the interface, which allows to control the size and aspect ratio of interfacial triangles [23]. Example of triangulations of the skin, skull and brain are shown on Figs. 1–3. Then, these triangulated surfaces together with a triangulation of the artificial boundary (absorbing boundary) of the overall computational domain are used as inputs for the generation of volume meshes. Finally, the GHS3-D tetrahedral mesh generator [24] is used to mesh the volume domains between the various interfaces. The exterior of the head must also be meshed, up to a certain distance. Then the computational domain is artificially bounded by a surface which defines the boundary Γ_a on which the Silver–Müller absorbing boundary condition is imposed. Moreover, a simplified mobile phone model (metallic box with a quarter-wave length mounted on the top surface) is included and placed in vertical position close to the right ear (see Fig. 4). The surface of this metallic box defines the boundary Γ_m. Overall, the geometrical models considered here consist of four tissues (skin, skull, CSF—Cerebro Spinal Fluid and brain).

IV. Numerical Results

A. Problem Setting

All the numerical experiments reported here are concerned with the propagation of an electromagnetic wave emitted by a dipolar source localized (and centered) between the lower tip of the antenna and the top surface of the metallic box, and is modeled by a current source term of the form ($\vec{x}_d$ is the localization point of the source)

$$\vec{J}_s(\vec{x},t) = f_0\delta(\vec{x}-\vec{x}_d)f(t)\vec{e}_z \tag{10}$$

where $f(t)$ is a sinusoidally varying temporal signal and f_0 is the amplitude of the signal. This source current is easily introduced and discretized according to the discontinuous Galerkin formulation discussed in Subsection II-B. The physical simulation time has been fixed to 5 periods of the temporal signal of (10). A discrete Fourier transform of the components of the electric field is computed during the last period of the simulation. The characteristics of the tissues are summarized in Table I where the values of the electrical permittivity correspond to a frequency $\mathrm{F} = 1800$ MHz. We first present and discuss numerical results obtained with a uniform approximation order

TABLE I
EXPOSURE OF HEAD TISSUES TO A LOCALIZED SOURCE RADIATION: ELECTROMAGNETIC CHARACTERISTICS OF TISSUES

Tissue	ε_r	λ (mm)	σ (S/m)	ρ (kg/m^3)
Skin	43.85	26.73	1.23	1100.0
Skull	15.56	42.25	0.43	1200.0
CSF	67.20	20.33	2.92	1000.0
Brain	43.55	25.26	1.15	1050.0

DGTD-$\mathbb{P}_p$ method (i.e., $\forall \tau_i \in \mathcal{T}_h$ we set $p_i = p$) and then consider the case of a nonuniform order DGTD-$\mathbb{P}_{p_i}$ method. One of the objectives of this numerical study is to show that the use of a nonuniform order DGTD-$\mathbb{P}_{p_i}$ method combined with appropriately coarsened geometrical models allows for a notable reduction of the computing time without sacrificing the accuracy of the results.

B. Numerical Assessment of the Stair-Casing Effect

As stated in the introductory part of this paper, the present work aims at studying an alternative numerical dosimetry methodology which allows for a realistic modeling of geometrical features and tissue interfaces in order to alleviate the stair-casing effect inherent to classical finite difference time-domain methods making use of Cartesian grids. We further discuss and illustrate numerically this effect here by focusing on two modeling situations: first, we consider a model test problem in 2-D for which an analytical solution exists and we compare the accuracy of calculations performed using DGTD methods designed on uniform quadrangular meshes on one hand, and on unstructured triangular meshes on the other hand; second, as a more realistic configuration in 3-D, we compare the approximate solution obtained using an industrial FDTD method [12] with that of the DGTD-$\mathbb{P}_p$ method discussed here, for the propagation in a heterogeneous model of head tissues.

1) Standing Wave in a 2-D Circular PEC Cavity: The first test problem aims at allowing a rigorous assessment of the stair-casing effect thanks to the availability of an analytical solution of the 2-D TMz Maxwell equations. Indeed, we consider a circular PEC resonator with radius $r = 0.5$ m. The exact time-domain solution of the problem is

$$\begin{cases} E_z = J_1(\omega r)\sin(\omega t + \theta) \\ H_x = \frac{y}{2r}[J_0(\omega r) - J_2(\omega r)]\cos(\omega t + \theta) - \frac{x}{\omega r^2}E_z \\ H_y = -\frac{x}{2r}[J_0(\omega r) - J_2(\omega r)]\cos(\omega t + \theta) - \frac{y}{\omega r^2}E_z \end{cases}$$

where $\omega = 42.1 \times 10^8$ m/s (F = 0.67 GHz), which is obtained from the PEC boundary condition $E_z = 0$ at $r = 0.5$ m; (r, θ) represents the usual polar coordinates and J_n (n is a positive integer) stands for the nth-order Bessel functions of the first kind. We compare approximate solutions obtained using a DGTD-$\mathbb{P}_p$ method formulated on a triangular mesh with those resulting from a DGTD-$\mathbb{Q}_p$ method formulated on an orthogonal quadrangular mesh. Three triangular meshes (MT1 to MT3 on the figures) have been considered with respectively 310, 1320, and 5654 elements. The minimal length of the edges of each mesh is respectively equal to 0.0412 m, 0.0131 m, and 0.0061 m. Similarly, three quadrangular meshes (MQ1 to MQ3 on the figures) have been used with respectively 241, 1109, and 4717 elements. These meshes are uniform with $\Delta x = \Delta y$ =0.0526 m, 0.0256 m, and 0.0126 m for each mesh respectively. Sample meshes are shown in Fig. 5. For this particular study, we limited ourselves to the case $p = 1$. We plot in Figs. 6 and 7 the time evolution respectively, of the L_2 error between the approximate and exact solutions, and of the E_z component. It is clearly seen on the plots of Fig. 6 and Fig. 7 that although the accuracy of the DGTD-$\mathbb{Q}_1$ calculations improves with finer discretizations it remains far from acceptable. In comparison, the approximate solution resulting from the DGTD-$\mathbb{P}_1$ method using mesh MT2 is close to the analytical solution.

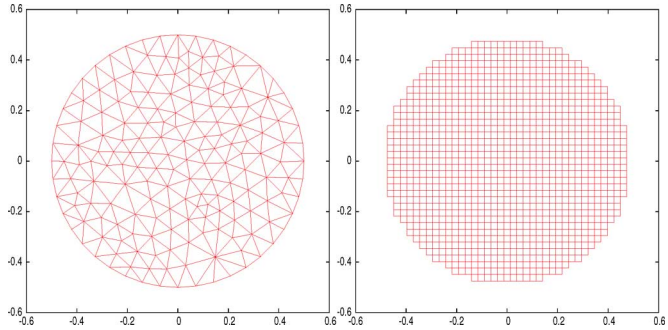

Fig. 5. Standing wave in a 2-D circular PEC cavity. Unstructured triangular meshes MT1 to MT3 (left figure) and uniform quadrangular meshes MQ1 to MQ3 (right figure).

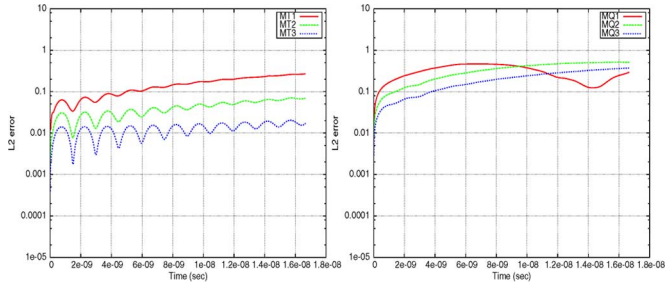

Fig. 6. Standing wave in a 2-D circular PEC cavity: time evolution of the L_2 error. Comparisons between the DGTD-$\mathbb{P}_p$ (left figure) and DGTD-$\mathbb{Q}_p$ (right figure) methods.

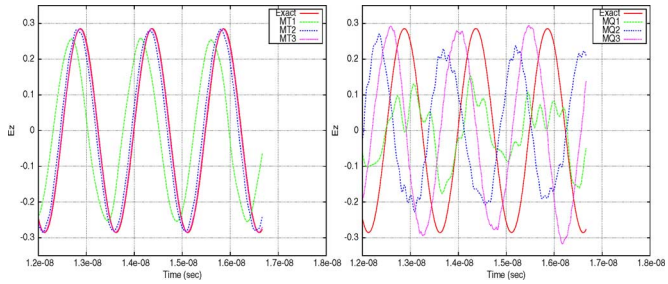

Fig. 7. Standing wave in a 2-D circular PEC cavity: time evolution of the E_z component. Comparisons between the DGTD-$\mathbb{P}_p$ (left figure) and DGTD-$\mathbb{Q}_p$ (right figure) methods.

2) Propagation in a 3-D Heterogeneous Head Model: In the second test problem, we consider an heterogeneous model of head tissues has described in Subsection IV-A but without taking into account the model mobile phone geometry in order to focus on the influence of the discretization of the interfaces between tissues. A dipolar source characterized by a current source term of the form (10) with $f_0 = 3.0 \times 10^{-18}$ A/m^2. We make use of a relatively coarse tetrahedral discretization of

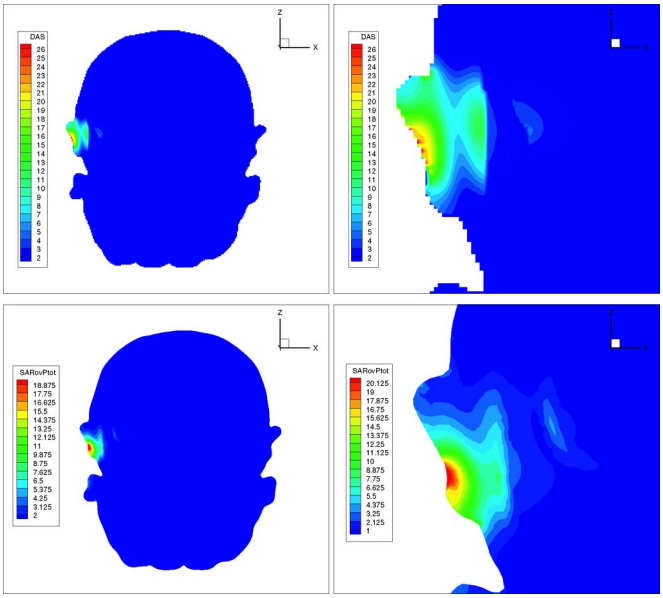

Fig. 8. Comparisons between the FDTD (top figures) and DGTD (bottom figures: DGTD-$\mathbb{P}_1$ method) methods. Contour lines of normalized local SAR (selected cut plane).

TABLE II
CHARACTERISTICS OF THE FULLY UNSTRUCTURED TETRAHEDRAL MESHES OF HEAD TISSUES

Mesh	# elements	L_{min} (mm)	L_{max} (mm)	L_{avg} (mm)
M1	815,405	1.00	28.14	10.69
M2	1,862,136	0.65	23.81	6.89
M3	7,894,172	0.77	22.75	3.21

the head tissues containing 7 162 936 elements. The minimum, maximum, and average lengths of the edges of this mesh are respectively equal to 0.63 mm, 3.11 mm, and 26.81 mm. A numerical simulation has been performed for a duration of 10 periods of the temporal signal of (10). The corresponding total emitted power is 1.36×10^{-14} W and the maximum value of the local SAR normalized to the total emitted power is 83.57 W/kg. The same problem has also been considered with a FDTD method [12] using a uniform Cartesian mesh with $\Delta x = \Delta y = \Delta z = 1$ mm, consisting of $96 \times 242 \times 232$ cells. The total emitted power is in this case 6.75×10^{-15} W and the maximum value of the local SAR normalized to the total emitted power is 76.92 W/kg. Contour lines of the local SAR normalized to the total emitted power plotted in a selected cut plane are compared in Fig. 8. Although the SAR patterns are globally similar we observe noticeable differences in the ear region. It is clear that the discretization of the air-skin interface in this region greatly impacts the local SAR pattern. In particular, we note that the maximum local SAR characterizing the DGTD-$\mathbb{P}_1$ method is almost 38% higher.

C. DGTD Results With Various Geometrical Models

1) Fully Unstructured Geometrical Models: We consider a sequence of three unstructured tetrahedral meshes whose characteristics are summarized in Table II. For these meshes, the artificial boundary Γ_a is a spherical surface approximately located one wavelength away from the skin. The tetrahedral meshes are globally nonuniform and the quantities L_{min}, L_{max}, and L_{avg} in Table II, respectively, denote the minimum, maximum, and average lengths of mesh edges. For the following simulations, we make use of a dipolar source characterized by a current source term of the form (10) with $f_0 = 10^{-9}$ A/m^2. Contour lines of the local SAR normalized to the maximum value of the local SAR are shown in Figs. 9–11 for calculations based on the coarsest mesh (i.e., mesh M1), and in Fig. 12 for a calculation based on the finest mesh (i.e., mesh M3). Besides, Fig. 13 portrays the contour lines of the local SAR normalized to the total emitted power for this latter calculation. Finally, Table III

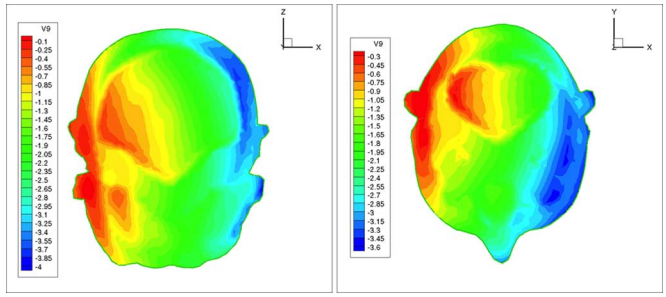

Fig. 9. Calculations with the DGTD-$\mathbb{P}_1$ method. Mesh M1: contour lines of local SAR over maximum local SAR in log scale (selected cut planes).

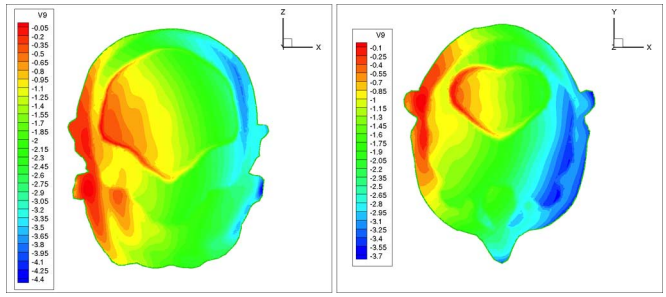

Fig. 10. Calculations with the DGTD-$\mathbb{P}_2$ method. Mesh M1: contour lines of local SAR over maximum local SAR in log scale (selected cut planes).

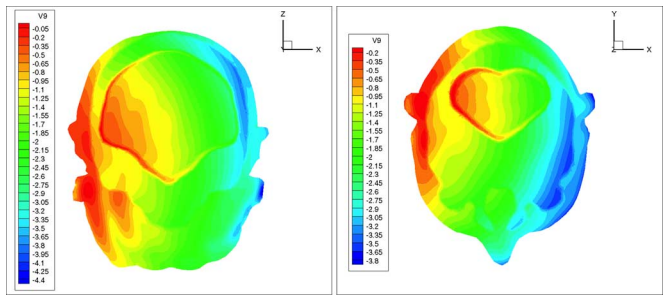

Fig. 11. Calculations with the DGTD-$\mathbb{P}_3$ method. Mesh M1: contour lines of local SAR over maximum local SAR in log scale (selected cut planes).

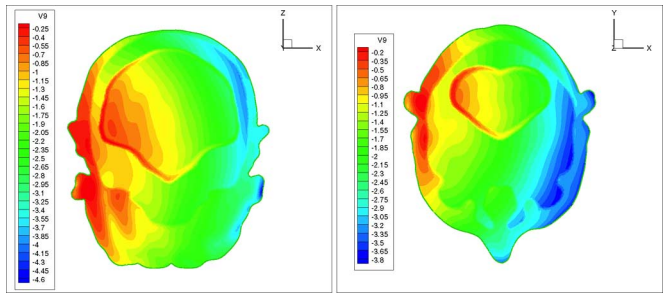

Fig. 12. Calculations with the DGTD-$\mathbb{P}_1$ method. Mesh M3: contour lines of local SAR over maximum local SAR in log scale (selected cut planes).

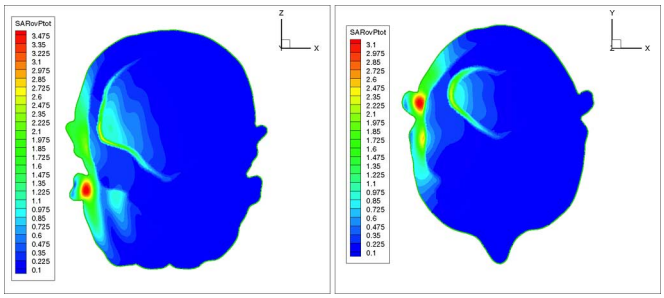

Fig. 13. Calculations with the DGTD-$\mathbb{P}_1$ method. Mesh M3: contour lines of normalized local SAR (selected cut planes).

TABLE III
CALCULATIONS WITH THE DGTD-$\mathbb{P}_p$ METHOD. MAXIMUM VALUE OF THE NORMALIZED LOCAL SAR

Mesh	Method
-	DGTD-$\mathbb{P}_1$
M1	3.365 W/kg (0.463, 12.1 %)
M2	3.734 W/kg (0.094, 2.4 %)
M3	3.828 W/kg (reference value)
-	DGTD-$\mathbb{P}_2$
M1	3.269 W/kg (0.559, 14.6 %)
M2	3.586 W/kg (0.242, 6.3 %)
-	DGTD-$\mathbb{P}_3$
M1	3.283 W/kg (0.545, 12.3 %)

summarizes the values of the local SAR normalized to the total emitted power.

In order to discuss these results, we consider that the numerical solution computed with mesh M3 using the DGTD-$\mathbb{P}_1$ method defines a reference solution. Patterns of the contour lines for calculations, respectively, performed with mesh M1 using the DGTD-$\mathbb{P}_3$ method and with mesh M3 using the DGTD-$\mathbb{P}_1$ method are very similar. However variations certainly exist locally since the ranges of the plotted values differ (especially for the local SAR normalized to the total emitted power). In Table III, the quantities given parenthetically are the difference with the reference value (i.e., the one associated to mesh M3 and the DGTD-$\mathbb{P}_1$ method) and the corresponding error level. We note here that the relative error tends to increase when switching from $p = 1$ to $p = 2$ for a given discretization mesh. Again, this should not be interpreted as a counter effect of an increase of the approximation order since this relative error is evaluated on the basis of a solution computed on the finest mesh which is based on high-resolution triangulations of the tissue interfaces (see the figures in Section III). Rather, we can surely conclude that the discretization of the geometrical features of tissues has a greater impact on accuracy than the interpolation order in the DGTD-$\mathbb{P}_p$ method (first column of Table III). Numerical simulations have been conducted on a Bull Novascale 3045 parallel system consisting of Intel Itanium 2/1.6 GHz nodes interconnected by a high-performance Infiniband network. Each node consists of a 8 core board with 21 GB of shared memory. Computing times are summarized in Table IV where the quantity given parenthetically is the number of cores used for the corresponding simulation. The parallelization of the DGTD-$\mathbb{P}_p$ solver is based on a single program multiple data (SPMD) strategy which combines a partitioning of the tetrahedral mesh using a graph partitioning tool (MeTiS [25] in the present case), with a message passing programming using the message passing interface (MPI) environment. Besides, for further comparisons with simulations performed on a high-end workstation that are discussed in Section IV-C2, we have also estimated the sequential computing time for the simulation based on mesh M3 and the DGTD-$\mathbb{P}_1$ method. This workstation is equipped with a Intel Xeon E5345/2.33 GHz CPU and 32 GB of RAM. The corresponding computing time is 936 hours (i.e., 39 days).

TABLE IV
CALCULATIONS WITH THE DGTD-$\mathbb{P}_p$ METHOD. COMPUTING TIMES

Mesh	Method
-	DGTD-$\mathbb{P}_1$
M1	553 sec (128 procs)
M2	239 sec (256 procs)
M3	761 sec (512 procs)
-	DGTD-$\mathbb{P}_2$
M1	708 sec (128 procs)
M2	1143 sec (256 procs)
-	DGTD-$\mathbb{P}_3$
M1	1862 sec (128 procs)

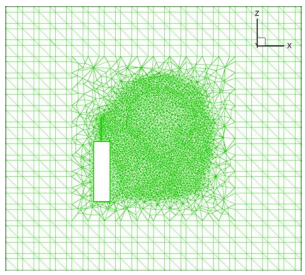

Fig. 14. Hybrid structured-unstructured tetrahedral mesh of head tissues.

2) Hybrid Structured-Unstructured Geometrical Models: The results obtained previously suggest that one should keep a sufficiently accurate representation of the geometrical features of the tissues and, in the regions where the mesh is refined and the discretization parameter is small, limit the approximation order to $p = 1$. Here, we investigate further this possibility by considering the use of hybrid structured-unstructured tetrahedral meshes which are built in the following way: 1) the artificial boundary Γ_a is defined as a plane-parallel surface; 2) we introduce a second plane-parallel surface, denoted by Γ_0, delimiting a volume which encompasses the head and the phone model; 3) the volume space between Γ_a and Γ_0 (vacuum space) is discretized using a uniform (structured) tetrahedral mesh; 4) the volume delimited by the surface Γ_0 is discretized using a nonuniform (unstructured) tetrahedral mesh. We stress that the resulting tetrahedral mesh is conforming, i.e., the same triangulated surface Γ_0 is used for the construction of the structured and unstructured parts of the tetrahedral mesh. Given this type of geometrical model, we consider now using a DGTD-$\mathbb{P}_{(p_1,p_2)}$ method where p_1 is the interpolation order for the approximation of the electromagnetic field in the elements of the unstructured part of the mesh while p_2 is adopted in the elements of the structured part. An example of such a mesh is shown in Fig. 14 (planar view in a selected plane). Note that the size of the elements in the structured part are intentionally kept relatively large. This motivates the use of a high interpolation

TABLE V
CHARACTERISTICS OF THE HYBRID STRUCTURED-UNSTRUCTURED TETRAHEDRAL MESHES OF HEAD TISSUES

Mesh	# elements	L_{min} (mm)	L_{max} (mm)	L_{avg} (mm)
M1h	398,220	0.91	86.60	7.63
M2h	458,458	0.91	53.56	9.66

TABLE VI
CALCULATIONS WITH THE DGTD-$\mathbb{P}_p$ AND DGTD-$\mathbb{P}_{(p_1,p_2)}$ METHODS. MAXIMUM VALUE OF THE NORMALIZED LOCAL SAR

Mesh	Method
-	DGTD-$\mathbb{P}_1$
M1h	3.719 W/kg (0.109, 2.8 %)
M2h	3.724 W/kg (0.181, 4.7 %)
-	DGTD-$\mathbb{P}_2$
M1h	3.557 W/kg (0.271, 7.1 %)
M2h	3.587 W/kg (0.241, 6.2 %)
-	DGTD-$\mathbb{P}_3$
M1h	3.542 W/kg (0.286, 7.4 %)
M2h	3.501 W/kg (0.327, 8.5 %)
-	DGTD-$\mathbb{P}_{1,2}$
M1h	3.733 W/kg (0.095, 2.5 %)
M2h	3.660 W/kg (0.168, 4.4 %)

TABLE VII
CALCULATIONS WITH THE DGTD-$\mathbb{P}_p$ AND DGTD-$\mathbb{P}_{(p_1,p_2)}$ METHODS. COMPUTING TIMES

Mesh	DGTD-$\mathbb{P}_1$	DGTD-$\mathbb{P}_2$	DGTD-$\mathbb{P}_{1,2}$
M1h	3 h 59 mn	19 h 12 mn	4 h 17 mn
M2h	3 h 6 mn	22 h 47 mn	7 h 12 mn

order in these elements; typically, in the following, we set $p_1 = 1$ and $p_2 > p_1$. The characteristics of the tetrahedral meshes that have been used for this study are summarized in Table V. These meshes are based on the surface triangulations of the tissues already used for the construction of mesh M2 of Table II. As previously, numerical simulations have been performed for a duration of 5 periods of the temporal signal of (10). Table VI summarizes the values of the local SAR normalized to the total emitted power. The error levels are again given with respect to the numerical solution obtained using the unstructured mesh M3 and the DGTD-$\mathbb{P}_1$ method (see Table III). Finally, computing times are given in Table VII. Overall, these results show that the numerical modeling strategy which consists in the association of a hybrid structured-unstructured geometrical model with a nonuniform order DGTD-$\mathbb{P}_{(p_1,p_2)}$ method offers a good compromise between accuracy and computing time of the simulation. For instance, for the calculation based on mesh M1h and the DGTD-$\mathbb{P}_{1,2}$ method, the relative error on the maximum value of the local SAR is 2.5% while the sequential computing time is reduced from 936 hours to less than 5 hours. However, we recall that the construction of mesh M2h is based on the surface triangulations of the tissues already used for the construction of mesh M2 of Table II; therefore, a more friendly comparison should involve a hybrid structured-unstructured mesh relying on the surface triangulations adopted for the construction of the fully unstructured mesh M3. Using such a mesh should lowered the gain in computing time with regards to a calculation with the fully unstructured mesh M3, but it should also improve the accuracy of the results.

V. CONCLUSION

In this work, we have performed a detailed assessment of the application of a high order DGTD method for the simulation of the propagation of an electromagnetic wave within unstructured tetrahedral mesh based geometrical models of head tissues. The distribution of the SAR and the maximum value of the local SAR have been used as a basis for comparisons of numerical solutions obtained using several geometrical models corresponding to the discretization of four tissues (skin, skull, CSF, and brain). In particular, we have studied the possibility of coarsening the discretization of tissue interfaces on one hand, and of combining structured (for the propagation in free space) and unstructured (for the propagation in the tissues) tetrahedral meshes on the other hand, in order to reduce the computing time of the simulation subjected to some target accuracy level. The DGTD method can easily handle such hybrid structured-unstructured geometrical models. In addition, it allows for a nonuniform definition of the approximation order and this has been exploited here only partially by defining different approximation orders for the structured and unstructured parts of a mesh. A first natural generalization of this DGTD-$\mathbb{P}_{(p_1,p_2)}$ formulation would be to allow for a definition of the approximation order at the element level based on an appropriate criterion. Ideally, this criterion should be based on some form of *a posteriori* error estimation; however, the obtention of such a criterion for the heterogenous time-domain Maxwell equations is still an opened question. Besides, the use of unstructured or hybrid structured-unstructured tetrahedral meshes incurs a reduction of the allowable time step for a stable explicit time stepping. This reduction of the time step is often due to only a small fraction of the elements of the mesh (typically less than 1%). In such situations, the efficiency of the DGTD-$\mathbb{P}_p$ method can be substantially improved by resorting to a hybrid explicit-implicit time stepping strategy. Such a strategy has been recently proposed in [26]. The proposed hybrid explicit-implicit DGTD-$\mathbb{P}_p$ method combines a leap-frog scheme with a Crank–Nicolson scheme and assumes a partitioning of the mesh elements into two sets based on a geometric criterion.

ACKNOWLEDGMENT

In memory of our friend and coauthor Man-Fai Wong who passed away last April. This work was granted access to the HPC resources of CCRT under the allocation 2009-t2009065004 made by GENCI (Grand Equipement National de Calcul Intensif).

REFERENCES

[1] P. Bernardi, M. Cavagnaro, S. Pisa, and E. Piuzzi, "Power absorption and temperature elevations induced in the human head by a dual-band monopole-helix antenna phone," *IEEE Trans. Microw. Theory Tech.*, vol. 49, no. 12, pp. 2539–2546, Dec. 2001.

[2] O. Gandhi, Q.-X. Li, and G. Kang, "Temperature rise for the human head for cellular telephones and for peak SARs prescribed in safety guidelines," *IEEE Trans. Microw. Theory Tech.*, vol. 49, no. 9, pp. 1607–1613, Sep. 2001.

[3] E. Conil, A. Hadjem, F. Lacroux, M. Wong, and J. Wiart, "Variability analysis of SAR from 20 MHz to 2.4 GHz for different adult and child models using finite-difference time-domain," *Phys. Med. Biol.*, vol. 53, pp. 151–1525, 2008.

[4] J.-C. Camart, D. Despretz, M. Chivé, and J. Pribetich, "Modeling of various kinds of applicators used for microwave hyperthermia based on the FDTD method," *IEEE Trans. Microw. Theory Tech.*, vol. 44, no. 10, pp. 1811–1818, Oct. 1996.
[5] D. Dunn, C. Rappaport, and A. Terzuoli, "FDTD verification of deepset brain tumor hyperthermia using a spherical microwave source distribution," *IEEE Trans. Microw. Theory Tech.*, vol. 44, no. 10, pp. 1769–1777, Oct. 1996.
[6] J. Lin, S. Hinrai, C. Chiang, W. Hsu, J.-L. Su, and Y. , "Computer simulation and experimental studies of SAR distributions of interstitial arrays of sleeved-slot microwave antennas for hyperthermia treatment of brain tumors," *IEEE Trans. Microw. Theory Tech.*, vol. 48, no. 11, pp. 2191–2198, Nov. 2000.
[7] J. Kim and Y. Rahmat-Samii, "Implanted antennas inside a human body: Simulations, designs, and characterizations," *IEEE Trans. Microw. Theory Tech.*, vol. 52, no. 8, pp. 1934–1943, Aug. 2004.
[8] K. Yee, "Numerical solution of initial boundary value problems involving Maxwell's equations in isotropic media," *IEEE Trans. Antennas Propag.*, vol. AP-16, no. 3, pp. 302–307, May 1966.
[9] A. Ditkowski, K. Dridi, and J. Hesthaven, "Convergent Cartesian grid methods for Maxwell's equations in complex geometries," *J. Comput. Phys.*, vol. 170, no. 1, pp. 39–80, 2001.
[10] K. Dridi, J. Hesthaven, and A. Ditkowski, "Staircase-free finite-difference time-domain formulation for general materials in complex geometries," *IEEE Trans. Antennas Propag.*, vol. 49, no. 5, pp. 749–755, May 2001.
[11] T. Xiao and Q. Liu, "A staggered upwind embedded boundary (SUEB) method to eliminate the FDTD staircasing error," *IEEE Trans. Antennas Propag.*, vol. 52, no. 3, pp. 730–741, Mar. 2004.
[12] S. Chaillou, J. Wiart, and W. Tabbara, "A subgridding scheme based on mesh nesting for the FDTD method," *Microw. Opt. Technol. Lett.*, vol. 22, no. 3, pp. 211–214, 1999.
[13] F. Collino, T. Fouquet, and P. Joly, "Conservative space-time mesh refinement methods for the FDTD solution of Maxwell's equations," *J. Comput. Phys.*, vol. 211, no. 1, pp. 9–35, 2006.
[14] J. Hesthaven, *High-Order Accurate Methods in Time-Domain Computational Electromagnetics: A Review*, ser. Advances in Imaging and Electron Physics. New York: Academic, 2003, vol. 127, pp. 59–123.
[15] A. Yefet and P. Petropoulos, "A staggered fourth-order accurate explicit finite difference scheme for the time-domain Maxwell's equations," *J. Comput. Phys.*, vol. 168, no. 2, pp. 286–315, 2001.
[16] Z. Xie, C.-H. Chan, and B. Zhang, "An explicit fourth-order orthogonal curvilinear staggered-grid FDTD method for Maxwell's equations," *J. Comput. Phys.*, vol. 175, no. 2, pp. 739–763, 2002.
[17] J. Hesthaven and T. Warburton, "Nodal high-order methods on unstructured grids. I. time-domain solution of Maxwell's equations," *J. Comput. Phys.*, vol. 181, pp. 186–221, 2002.
[18] L. Fezoui, S. Lanteri, S. Lohrengel, and S. Piperno, "Convergence and stability of a discontinuous Galerkin time-domain method for the 3-D heterogeneous Maxwell equations on unstructured meshes," *ESAIM: Math. Model. Numer. Anal.*, vol. 39, no. 6, pp. 1149–1176, 2005.
[19] G. Cohen, X. Ferrieres, and S. Pernet, "A spatial high-order hexahedral discontinuous Galerkin method to solve Maxwell's equations in time domain," *J. Comput. Phys.*, vol. 217, pp. 340–363, 2006.
[20] H. Fahs, "Development of a hp-like discontinuous Galerkin time-domain method on non-conforming simplicial meshes for electromagnetic wave propagation," *Int. J. Numer. Anal. Mod.*, vol. 6, pp. 193–216, 2009.
[21] P. Ratiu, B. Hillen, J. Glaser, and D. Jenkins, *Medicine Meets Virtual Reality 11—NextMed: Health Horizon*. Amsterdam, The Netherlands: IOS Press, 2003, vol. 11, ch. Visible Human 2.0—The next generation, pp. 275–281.
[22] L. Chew, "Guaranteed-quality mesh generation for curved surfaces," in *9th Annu. ACM Symp. Comput. Geometry*, 1993, pp. 274–280, ACM Press.
[23] J.-D. Boissonnat and S. Oudot, "Provably good sampling and meshing of surfaces," *Graphical Models*, vol. 67, no. 5, pp. 405–451, 2005.
[24] P.-L. George, F. Hecht, and E. Saltel, "Automatic mesh generator with specified boundary," *Comput. Methods Appl. Mech. Eng.*, vol. 92, pp. 269–288, 1991.
[25] G. Karypis and V. Kumar, "Parallel multilevel k-way partition scheme for irregular graphs," *SIAM Rev.*, vol. 41, no. 2, pp. 278–300, 1999.
[26] V. Dolean, H. Fahs, L. Fezoui, and S. Lanteri, "Locally implicit discontinuous Galerkin method for time domain electromagnetics," *J. Comput. Phys.*, vol. 229, no. 2, pp. 512–526, 2010.

Hassan Fahs was born in 1981. He received the B.S. degree in mathematics from the Lebanese University, Beirut, and the Ph.D. degree in applied mathematics from the University of Nice-Sophia Antipolis, France, in 2008.

In 2009, he was a Postdoctoral Researcher at the French Institute of Petroleum. Since 2010, he has been a Research Engineer in the OSA Department, XLIM Institute, Limoges, France. His current research interests include computational electromagnetics with an emphasis on high-order finite-element methods, nonconforming methods, and the design of high-order time integrators for stiff ODEs.

Abdelhamid Hadjem received the Engineer degree in electrical engineering from the Science and Technology University, Algiers, Algeria, in 1999 and the M.Sc. degree in electronics and the Ph.D. degree in electrical engineering from Pierre and Marie Curie University (Paris VI), Paris, France, in 2001 and 2005, respectively.

Since 2006, he has been with the Research and Development, France Telecom, Issy les Moulineaux, France. His current research interests include electromagnetics for telecommunications systems and biomedical application of numerical electromagnetic techniques.

Stéphane Lanteri received the Ph.D. degree in engineering sciences from the University of Nice-Sophia Antipolis, Sophia Antipolis, France, in 1991.

He joined the INRIA Sophia Antipolis-Méditerranée Research Center in November 1993 and is currently a Senior Research Scientist in this institute. Since July 2007, he has been the scientific head of the Nachos project-team whose research activities are concerned with the development and application of numerical methodologies for the modeling of electromagnetic wave propagation in complex domains and heterogeneous media. His research interests are concerned with the design of unstructured mesh based high-order finite-element methods, efficient and accurate time integration methods, and numerical algorithms adapted to modern high-performance computing platforms. Since 2003, he has been involved in several national multi-partner projects dealing with the numerical modeling of human exposure to electromagnetic wave radiation from wireless communication systems.

Joe Wiart (M'96–A'01–SM'02) received the Engineer degree from the Ecole Nationale Supérieure des Télécommunications (ENST), Paris, France, in 1992, and the Ph.D. degree in physics from ENST and University of Pierre and Marie Curie, Paris, in 1995.

In 1992, he joined the Centre National d'Etude des Télécommunications (CNET), France Telecom, Issy les Moulineaux, France, where he was involved in the research on propagation in microcellular environment for three years. Since 1994, he has been involved in research on the interaction of radio waves with the human body and on medical electronic devices. He is currently the Head of the WHIST Lab, common laboratory of the Telecom Institute and Orange Labs (formerly CNET). His research interests include electromagnetic compatibility, bioelectromagnetics, antenna measurements, computational electromagnetics, statistics, and signal processing.

Dr. Wiart is an Emeritus member of the Societé de l'Electricité, de l'Electronique et des Technologies de l'Information et de la Communication. He was the Vice Chairman of the European Cooperation in Science and Technology (COST) 244 bis, a member of the Steering Committee of COST 281, and is involved in the new COST action BM0704. He is the Chairman of the European Committee for Electrotechnical Standardization (CENELEC) Working Group in charge of mobile and base-station standards. He is the President of the French chapter of the Union Radio Scientifique Internationale, France.

Man-Fai Wong (S'92–M'93–SM'99) received the Engineering Diploma degree in electronics from the Ecole Nationale d'Electronique, d'Electrotechnique, d'Informatique et d'Hydraulique et des Télécommunications, Toulouse, France, in 1990, and the Ph.D. degree in electrical engineering from Paris 7 University, Paris, France, in 1993.

From 1990 to 2011, he was with the Centre National d'Etude des Telecommunications (CNET), Issy les Moulineaux, France, (also known as France Telecom Research and Development (R&D), and now, Orange Labs, R&D), where he was involved in research in the fields of applied electromagnetic for telecommunications systems. From 1997 to 2011, he was engaged in research on the interactions of radio waves with human bodies of wireless systems. From 2008 to 2011, he lead the research program on sustainable development that includes the impact of electromagnetic fields on human bodies, the energy and environmental impact of telecom networks and terminals, as well as the use of ICT in sustainable development.

Dr. Wong was the Vice President of the Commission B of the Union Radio Scientifique Internationale, France, a Senior Member of the Société de l'Electricité et de l'Electronique (SEE), and the Chair of the French IEEE Chapter on Antennas and Propagation.